Towards a fast-running method for blast-wave mitigation by a prismatic blast wall

Sébastien Éveillard [a,b], Nicolas Lardjane [a,*], Jean-Yves Vinçont [a], Isabelle Sochet [b]

[a] CEA, DAM, DIF, Bruyères-le-Châtel, 91297 Arpajon, France
[b] Laboratoire PRISME – École nationale supérieure d'ingénieurs de Bourges, 88, bd Lahitolle, 18020 Bourges, France

A B S T R A C T

A procedure aimed at developing a fast-running method for blast-wave effects characterization behind a protection barrier is presented. Small-scale experiments of a hemispherical gaseous charge (stoichiometric propane–oxygen mixture) without and with a prismatic protective barrier are used to validate the use of an in-house CFD code for gaseous detonation. From numerical experiments, pressure loss of a blast wave at a corner is quantified. These fits, in conjunction with TM5-1300 reflection charts, are used to estimate the maximum overpressure around a protective barrier through geometrical and empirical laws. The results show good agreement with numerical and experimental data from the ANR-BARPPRO research project.

© 2013 Académie des sciences. Published by Elsevier Masson SAS. All rights reserved.

1. Introduction

Quantification of explosion effects has been an active subject of research for many years, see [1–3] for a review. The sudden release of a finite quantity of energy in air leads to the formation of a supersonic shock-wave whose amplitude, i.e. pressure jump, is smeared out with distance. A gauge, located at some distance from an ideally spherical explosive source, would record a static pressure signal, as sketched in Fig. 1. When the shock reaches the gauge, the pressure rises to a maximum and then decreases in a nonlinear way, crossing the ambient rest value (P_0) and defining a positive phase, then returning to a steady state at long times. In practice, the pressure signature is described by characteristic parameters: ΔP^+ (maximum overpressure), t_0 (arrival time), t^+ (positive phase duration), and some others, which are not necessary for this work.

Early studies helped to establish empirical laws between those parameters and have shown that different configurations can be compared with each other using Hopkinson's similitude parameter [4]. Small-scale experiments can then be used to obtain valuable information on complex industrial configurations such as the area effects as defined by the French regulation [5], Table 1.

In order to reduce explosion hazard due to accidental or intentional detonation, protection barriers may be used [3]. Those heavy weighted structures act like deflectors and protect people from thermal and ejection effects. The protection against overpressure effects is not guaranteed and is the goal of the ANR BARPPRO research program [6]. The difficulty lies in the interaction of the blast waves with a finite-length safety barrier. The wave's reflection, diffraction and self-interaction have to be taken into account to predict the location of shadow effect zones.

---

* Corresponding author. Tel.: +33 169264000.
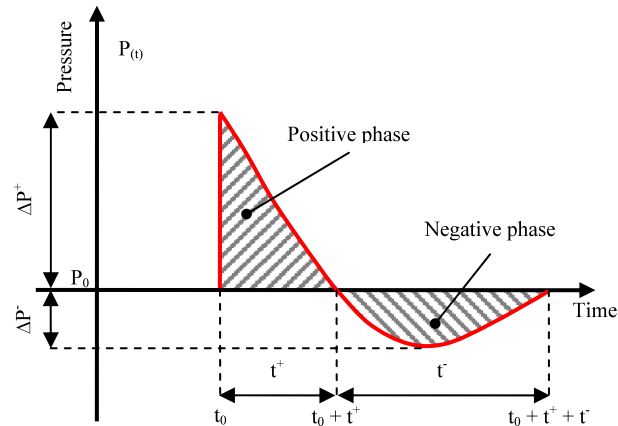 *E-mail address:* nicolas.lardjane@cea.fr (N. Lardjane).

Fig. 1. Schematic time history profile recorded at a gauge after an explosion.

Table 1
Classification of the effects areas by the French regulation [5].

Zone definition	Z_1	Z_2	Z_3	Z_4	Z_5
Impact on human	Extremely serious (fatal injuries in 50% cases)	Serious	Severe	Significant	Indirect effects through broken glass
Foreseeable damage to structure	Extremely serious	Important. Potential domino effect	Serious	Light	Significant destruction of windows
Overpressure range	$\Delta P^+ \geqslant 0.43$ bar	$\Delta P^+ \geqslant 0.20$ bar	$\Delta P^+ \geqslant 0.14$ bar	$\Delta P^+ \geqslant 0.05$ bar	$\Delta P^+ \geqslant 0{,}02$ bar

At the moment, only expensive three-dimensional computational fluid dynamics (CFD) techniques are able to accurately predict blast loads [7]. They are unfortunately out of reach for engineering applications and only few attempts were made to develop fast-running models. A promising way is the use of neural networks [8]. Nevertheless, this method is still under development in 2D configurations, since it needs an important amount of reliable data points to train the network and extrapolation to other configurations has to be proven. Another approach, closer to engineering interest, is the mix of cost-free geometrical laws and reflection charts [9,10]. From the best of the authors' knowledge, this methodology is limited to 2D configurations. It has only been applied in 3D, with some limited success, to estimate the pressure on the walls of a parallelepiped structure [11].

In this study, we present an extension of this second approach to obtain an approximation of the maximum overpressure at some distance from a prismatic protective wall (Section 3). This fast-running method is built and validated (Section 4) by the use of 3D numerical simulations and experimental results (Section 2).

2. Experimental and numerical investigations

Hopkinson's scaling law [4] was used to design small-scale experiments. In the case of a gaseous charge, reduced distance (λ) is defined by $\lambda = r/E^{1/3}$, where r is the distance from the charge's center and E is the energy released by the combustion of the charge. For a 1-m^3 sphere of stoichiometric propane–oxygen mixture, we have $E = 15.2$ MJ, which is energetically equivalent to a mass of 3.24 kg of TNT. One should note that pressure effects are different between a condensed explosive and a gaseous one [12]. In the following, we show results for a 0.12-m diameter sphere (about 2.9 g of TNT), located at 0.085 m from the middle line of a realistic safety barrier.

2.1. Experimental setup

Experiments were conducted in the PRISME laboratory located at Bourges, France. A sketch of the setup is given in Fig. 2, where α_1 is the front side inclination angle of the barrier, α_2 is the back side inclination angle, H is the height of the barrier, e is the top thickness, L is the transversal length, and d is the distance between the charge's center and the front side of the barrier. In this paper, for the sake of clarity, only results from Fig. 2's configuration are presented.

In practice, the gas mixture is injected in a soapy solution and forms a 0.12-m explosive half-bubble on the ground. Detonation is ignited by a high-voltage device, leading to the explosion of a thin metallic wire. Pressure history is recorded by piezo-electric transducers. Two reference sensors, located in the free-field part (no obstacle), allow us to determine the experimental uncertainty and confirm the reproducibility of each shot. Six other sensors, named S1 to S6, are set around the protective barrier as shown in Fig. 3 and Table 2. Their locations, on the ground ($y = 0$ m), around the back diffraction zone, give a valuable reference used for the validation of the CFD numerical results.
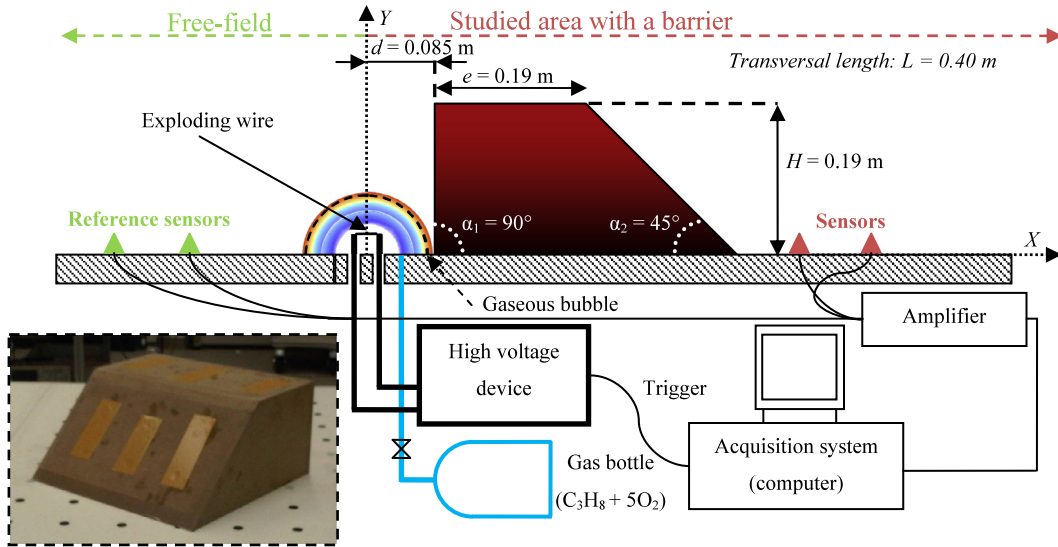
Fig. 2. (Color online.) Experimental bench and an experimental barrier studied with a gaseous explosion.
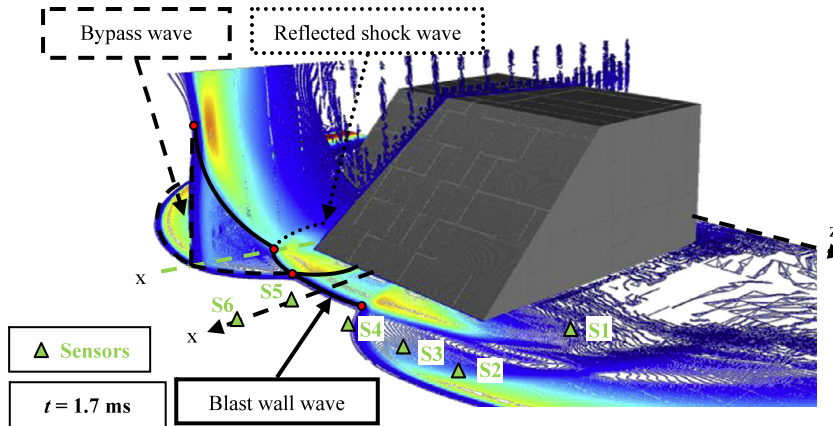

Fig. 3. (Color online.) Sensor locations around the protective barrier and pressure contours in two planes from a 3D numerical simulation. Note the complexity of the wave front.
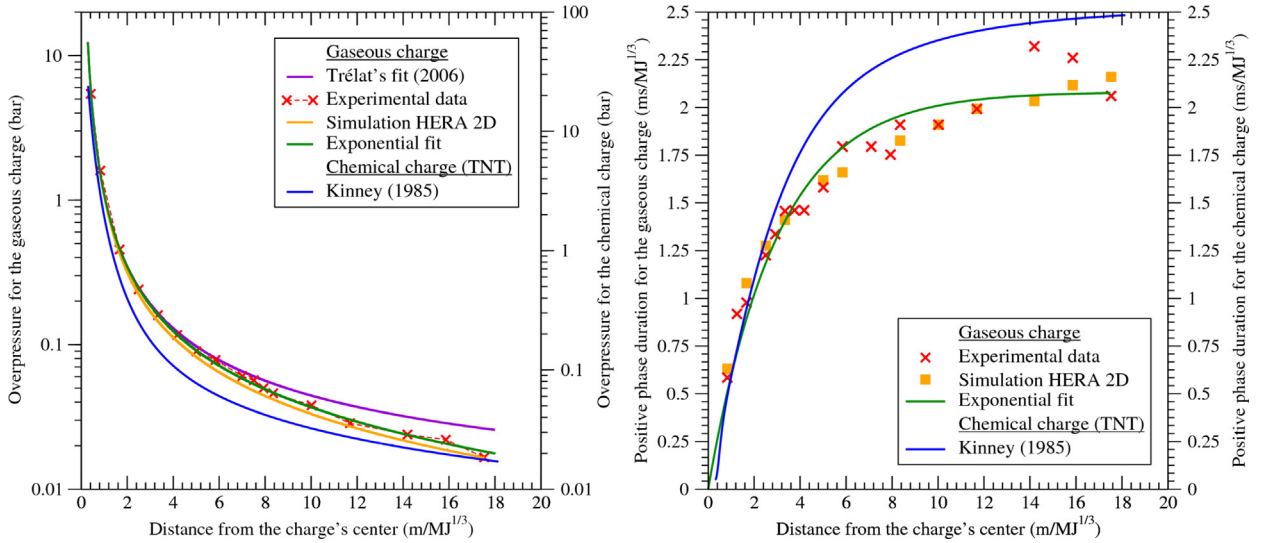
Table 2
Sensors' locations around the protective wall.

Sensor	S1	S2	S3	S4	S5	S6
X (m)	0.40	0.60	0.60	0.60	0.60	0.70
Z (m)	0.30	0.30	0.20	0.10	0.00	0.00

2.2. Comparison with numerical results

The HERA CFD software [13] was run on the TERA-100 supercomputer [14]. This multi-physics code uses adaptive mesh refinement (AMR), which helps reducing the amount of computational work when dealing with spatially moving discontinuities. HERA is well validated for TNT simulations [15].

In a first time, we validated an in-house gaseous explosive equation of state [16] for a propane–oxygen mixture by comparison with free-field experiments. For this purpose, 2D axisymmetric simulations are sufficient and an ultra-fine grid was used. We used three AMR levels, with a refinement factor of 3 and a fine cell size of 0.8 mm/MJ$^{1/3}$. Only refinement was allowed (no cell merging). The simulation results are compared to the free-field experimental data in Fig. 4 for the maximum overpressure and the duration of the positive phase versus the distance to the charge's center. The comparison is excellent showing a maximum deviation of 13%, which is at the same level as the measured experimental uncertainty of $\pm$10% on ΔP^+ and t_0 from one shot to the other.

Fig. 4. (Color online.) Spatial evolutions of maximal overpressure and positive phase duration for a stoichiometric propane–oxygen gaseous explosion in free field. Chemical TNT curves [4] are given for comparison.

Table 3
Comparison of the maximum overpressure for the first two events of each sensor.

Sensors	First peak			Second peak		
	Experiment	Simulation	Deviation	Experiment	Simulation	Deviation
S1	0.124 bar	0.128 bar	3.2%	None	None	None
S2	0.087 bar	0.081 bar	−7.4%	0.043 bar	0.053 bar	23.3%
S3	0.046 bar	0.043 bar	−7.0%	0.089 bar	0.080 bar	−10.1%
S4	0.029 bar	0.026 bar	−10.3%	0.107 bar	0.085 bar	−20.6%
S5	0.075 bar	0.059 bar	−21.3%	0.091 bar	0.096 bar	5.5%
S6	0.068 bar	0.055 bar	−19.1%	0.101 bar	0.099 bar	−2.0%

Empirical laws can then be derived, in free field, for the arrival time t_0, maximum overpressure ΔP_i^+, and positive phase duration t^+. These fits are valid for $0.84 \leqslant \lambda \leqslant 17.5$ m/MJ$^{1/3}$.

$$\ln\left(\frac{\Delta P_i^+}{P_0}\right) = 0.0895 - 1.7633\ln(\lambda) + 0.1528\ln(\lambda)^2 - 0.0066\ln(\lambda)^3 - 0.0021\ln(\lambda)^4 \tag{1}$$

$$\frac{t_0}{E^{1/3}} = 2.2937 \cdot 10^{-4}\lambda^4 - 9.6799 \cdot 10^{-3}\lambda^3 + 0.1437\lambda^2 + 1.9805\lambda - 0.7059 \tag{2}$$

$$\frac{t^+}{E^{1/3}} = 2.081\left(1 - e^{-0.3361\lambda}\right) \tag{3}$$

In a second time, 3D simulations of the barrier effect were performed on two meshes. Both use five AMR levels with an in cell refinement factor of 2. They differ on the finest cell size: 2.1 mm/MJ$^{1/3}$ for the fine mesh and 4.2 mm/MJ$^{1/3}$ for the coarse one. Simulations were run up to 2.5 ms on 256 and 1536 processors of TERA-100 for the coarse and fine meshes, leading to a maximal cell number of 159 million and 1.1 billion, respectively. Without CEA's computing facilities, the fine mesh case would have run nearly 1800 days on a single processor and 128 days for the coarse mesh case. Numerical results are compared with the experimental data for each previous sensor. Free-field sensors indicate a signal attenuation lower than 10% in comparison to the ultra-fine 2D simulations. As an example, the S3 record is plotted in Fig. 5. One should note the signal difference with or without the barrier. At this specific place, the maximum overpressure is lowered by more than a factor 2 behind the protective barrier. For the barrier case, we recorded two distinct events due to diffraction and reflection processes of the blast wave interacting with the protective barrier, see Fig. 3. For each event, the maximum overpressure is given in Table 3. We observed a maximum relative error lower than 10% for t_0 and of 23% for ΔP^+. This deviation is judged satisfactory, since the signal is the combination of several waves, for which only a 10% precision is expected in free field. Our 3D fine numerical simulation is thus legitimized and becomes a valuable tool for designing fast-running methods in the presence of protective barriers.
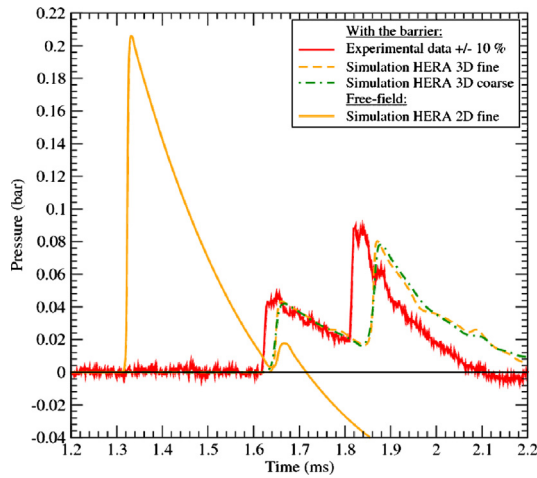
Fig. 5. (Color online.) Temporal evolution of pressure for the sensor S3.
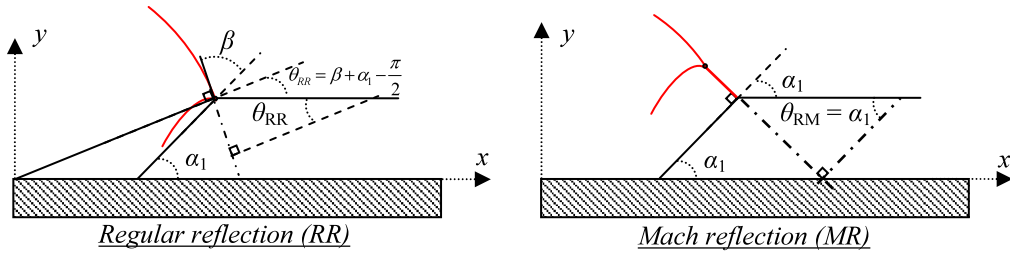

Fig. 6. Sketch of the influence of the reflection on the front side of a barrier.

3. Design of a fast-running method

The analysis of the sensors' records, cf. Fig. 5, shows that several distinct signals overlap, which suggests considering a superposition of waves coming from every side of the barrier. We thus need to characterize accurately the reflection and diffraction phenomena. Furthermore, since the pressure signal decreases rapidly with distance (1), the definition of a broken line path from the source to the observation point is a key ingredient of a fast-running method. In this section, we consider a general prismatic barrier with parameters defined in Section 2.1 and Fig. 2.

3.1. Reflection phenomenon

It is well known that the interaction of an unsteady shock-wave with an infinite rigid surface produces either a regular (RR) or Mach reflection (MR) [17], which increases the maximum overpressure behind the wave. For our case, the blast wave first reflects on the front side of the protection barrier, diffracts around corners and reflects again on the ground.

The kind of reflection depends on two main parameters of different nature: the blast incident Mach number (M_i) and the geometrical angle of incidence (β) between the shock and the rigid surface. The reflected front will then diffract over a structure corner; so it is mandatory to characterize the local front angle as sketched in Fig. 6.

Semi-empirical laws can be used to find the kind of reflection. For example, for a point on the front side of the barrier located at some distance from the charge's center, the incident overpressure (ΔP_i^+) is assessed, for a gaseous charge, by formula (1). From the Rankine–Hughoniot laws in air (perfect gas with $\gamma = 1.4$), the incident Mach number (M_i) is:

$$M_i = \sqrt{\frac{1}{2\gamma}\left[(\gamma+1)\frac{\Delta P_i^+ + P_0}{P_0} + \gamma - 1\right]} \tag{4}$$

This incident Mach number and the geometrical incidence angle (β), calculated from the dimensions of the studied configuration (d, α_1 and H), are then compared to the empirical Mach reflection limit (M_{iT}) of Kinney [4], which states:

$$M_{iT} = \frac{1.75}{\beta - 39} + 1 \quad \text{for } \beta \geqslant 39.7° \tag{5}$$
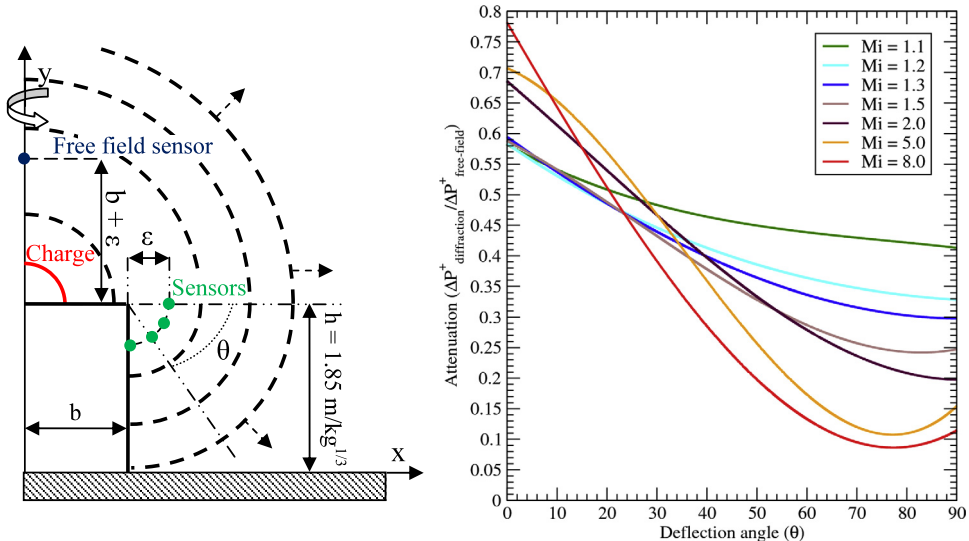
Fig. 7. (Color online.) Abacus of the diffraction coefficients with the numerical results.

If the incident Mach number (M_i) is greater than the limit Mach number (M_{iT}), the Mach stem appears on the front side of the barrier. The reflected overpressure ($\Delta P_r^+ = C_r \cdot \Delta P_i^+$) is simply estimated by digitized TM5-1300 abacus [18] in terms of the incidence angle (β) and incident overpressure (ΔP_i^+).

The kind of reflection on the front side defines the deflection angle and the type of blast wave (Mach reflection: Mach stem, regular reflection: incident wave) which is subject to a diffraction phenomenon on the top and back sides of the barrier.

3.2. Diffraction phenomenon

When the blast-wave reaches an edge of the barrier, it diffracts, decreasing the intensity of the shock (maximum overpressure). It is worth mentioning that unsteady shock-wave diffraction is more complicated than classical supersonic steady ones, since the speed of sound changes rapidly in the positive phase and an unsteady vortex emerges at the corner [4].

The shock intensity reduction depends on the geometrical deflection angle (θ), calculated as a function of the barrier parameters (d, α_1, α_2, e and H), and the incident Mach number subject to diffraction (M_d). As for the reflection case, the fast-running method requires diffraction abacus as a function of this two parameters. We created it numerically for several incident Mach numbers ranging from 1.1 to 8.0, freely diffracting over a 90° corner. The diffraction coefficient (C_d) is defined as the ratio of the diffracted wave overpressure and the free-field one for the same distance between the center of the charge and the observation point (distance λ).

Those simulations were performed with the HERA software for a 1-kg TNT chemical source in a 2D-axisymmetric approach, see Fig. 7. Sensors were located every 10° at $\varepsilon = 0.015$ m/kg$^{1/3}$ from the structure corner. The incident Mach number variation is obtained by changing the location (b) of the charge. We checked that other sensor locations did not affect the results.

The resulting abacus, see Fig. 7 right, shows a coefficient variation between 0.1 and 0.8. It extends the results of Miller [11], who used a single coefficient ($C_r = 0.35$) based on the estimation of [19].

3.3. Geometrical approach

Most fast-running models rely on the idea that the ray travelling the shortest distance from the source to an observation point is the most damaging [11]. Nevertheless, in the case of a 3D finite-length barrier, several rays can reach the target point nearly at the same time, requiring some summation. In this study, we consider both the direct wave from the source to any point plus rays generated through lateral diffraction effects, also named bypass waves.

From a geometrical point of view, direct waves split the studied configuration in several sectors, as shown in Fig. 8. The boundary between each sector is determined by a generic angle, Γ_i, depending on the barrier parameters (d, e, H, L, α_1, and α_2). Table 4 sums up the expected events in each sector. As previously stated, bypass waves, arising from diffraction at a corner, add two new sectors at each edge, which should be taken into account.
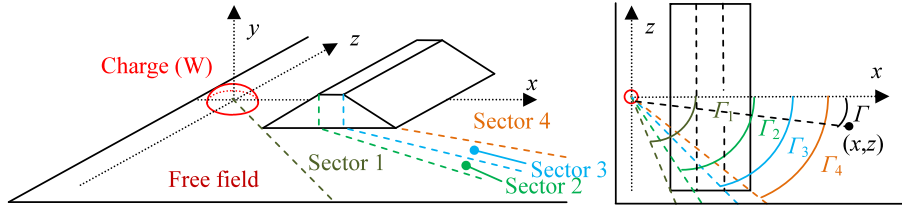
Fig. 8. (Color online.) Geometrical definition of sectors around the barrier for the direct wave.

Table 4
Physical phenomena description as a function of the sectors.

Blast wave	Free field	Sector 1	Sector 2	Sector 3	Sector 4
Straight line direct wave (over the barrier)	No direct interaction with the barrier	Reflection on the front side + diffraction on the corner of the front side + reflection the ground	Reflection on the front side + two-step diffraction + reflection on the ground		
Bypass wave	One diffraction on the corner of the barrier				Two diffractions between the corner for the front and back sides

3.4. Fast-running algorithm description

For the sake of simplicity, we assume a symmetric problem, i.e. a source located on the symmetry plane of the protective barrier.

As already discussed, at some observation point from the source, we determine two kinds of arrival: direct and bypass. We assume that each wave motion is independent from the other and they sum in pressure intensity at the target location. This hypothesis is a simplification of the LAMB rules depicted in [10]; it will reveal sufficient for this first version of our fast-running method. No clearing effect is included. For far field targets, we thus expect a pressure overestimation by a factor two, which is not restricting for security areas specification. Those crude approximations will be enhanced in future work.

The summation takes into account the temporal pressure decay behind the shock-wave assuming a modified Friedlander model for the positive phase [20]:

$$P(\lambda, t) = \Delta P_{\max}(\lambda) \times \left[1 - \frac{t - t_0(\lambda)}{t^+(\lambda)}\right] \times \exp\left[-C(\lambda)\frac{t - t_0(\lambda)}{t^+(\lambda)}\right] \tag{6}$$

The arrival time, t_0, and positive phase duration, t^+, are assumed direct functions of the distance, λ, as expressed by formulas (2) and (3). C is the non-dimensional decay coefficient which fits, for the propane–oxygen mixture, as:

$$C(\lambda) = 1.11 \cdot \lambda^{-0.62} \quad \text{for } 0.84 \leqslant \lambda \leqslant 17.5 \text{ m/MJ}^{1/3} \tag{7}$$

Determination of $\Delta P_{\max}$ is now explained.

3.4.1. Bypass wave overpressure

Characterization of $\Delta P_{\max}$ for the bypass wave requires the knowledge of reflection attributes (RR or MR) on any corner of the barrier and two diffractions coefficients ($C_{d_{b1}}$ and $C_{d_{b2}}$), as shown in Fig. 9.

For any ground point located at (x, y), one has to first determine the membership sector. For the sectors 1–2–3–4 bis, the bypass wave is subject to a unique diffraction at edge A, leading to the diffraction pressure coefficient $C_{d_{b1}}$ in A. The value of this coefficient depends on the angle of the shock-wave with the corner. We thus have to determine the kind of reflection on the front side of the barrier in conjunction with the reflected pressure coefficient C_{r_b}.

The incident overpressure at point A is estimated from formula (1) with the distance between the centre of the charge and this point (λ_A) as input.

$$\lambda_A = \sqrt{\left(\frac{L}{2}\right)^2 + d^2} \tag{8}$$

The incident angle on the corner of the barrier is denoted β_d. The reflection coefficient, C_{r_b}, is obtained from the TM5-1300 abacus, while the deviation angle, θ_{b1}, is evaluated this way:

$$\theta_{b1,MR} = \arctan\left(\frac{x - d}{z - L/2}\right) \quad \text{for Mach reflection} \tag{9}$$

$$\theta_{b1,RR} = \theta_{b1,MR} - \arctan\left(\frac{2d}{L}\right) \quad \text{for regular reflection} \tag{10}$$
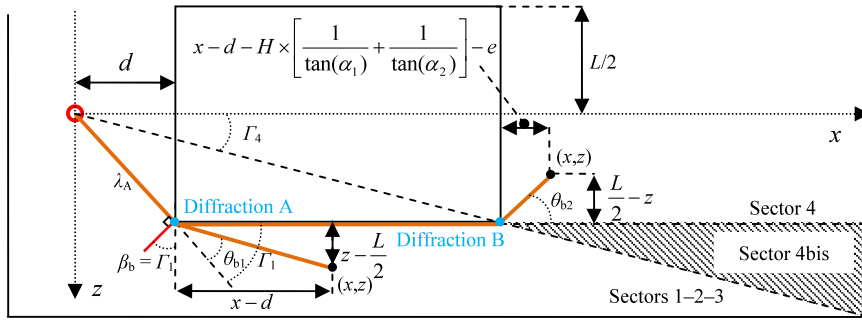
Fig. 9. (Color online.) Representation of the geometrical parameters for the bypass wave.
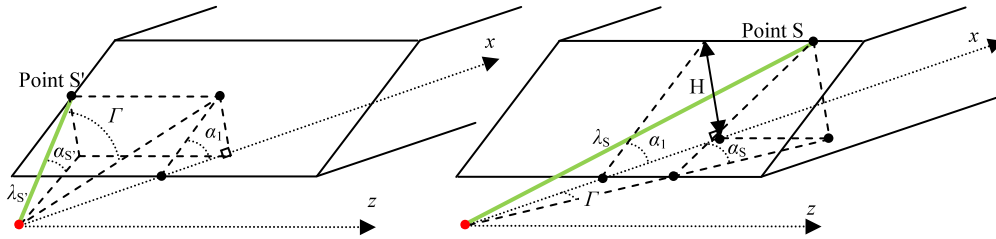

Fig. 10. Front face intersection by the direct wave.
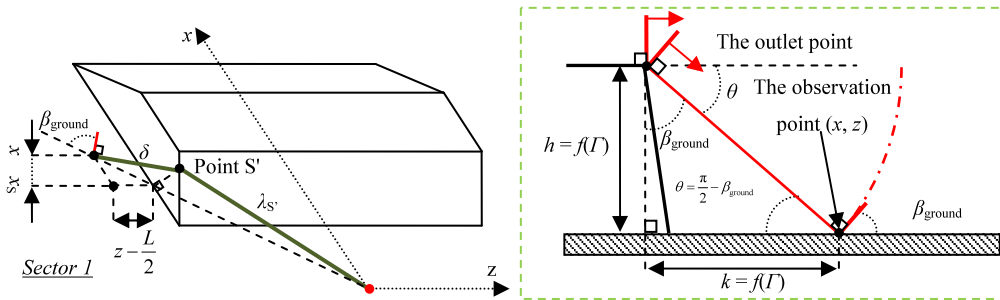

Fig. 11. Side diffraction and ground reflection.

The incident overpressure at point B is estimated from formula (1), using the distance between the centre of the charge and point B(λ_B) and the previous coefficients ($C_{d_{b1}}$ and C_{r_b} in case of a Mach reflection on the front side). The effective distance is then:

$$\lambda_B = \lambda_A + e + H \times \left[\frac{1}{\tan(\alpha_1)} + \frac{1}{\tan(\alpha_2)} \right] \tag{11}$$

And the deflection angle (θ_{b2}) reads:

$$\theta_{b2} = \arctan\left[\frac{L/2 - z}{x - \left(d + e + H \times \left(\frac{1}{\tan(\alpha_1)} + \frac{1}{\tan(\alpha_2)}\right)\right)} \right] \tag{12}$$

The final distance between the source's center and any observation point is denoted d_b. The bypass wave maximum overpressure (ΔP_b^+) is estimated from the previous coefficients, assuming an unaltered positive phase, as:

$$\Delta P_b^+ = \Delta P_i^+(d_b) \times Cr_b \times \prod_k C_{d_{bk}} \tag{13}$$

3.4.2. Direct wave overpressure

The estimation of the direct wave overpressure first necessitates determining on each surface the output point of the barrier for any ray of interest. This point is used to determine the kind of reflection and the reflection coefficient as previously explained. Elementary ray paths on each sector are drawn in Figs. 10–12.

As an example, on the front side (Fig. 10), two cases may happen. When the ray wave leaves the side, an exit point, labeled S' or S, appears, alimenting sectors 1 and 2–3–4, respectively. The determination of the reflection coefficient (C_{r_s})

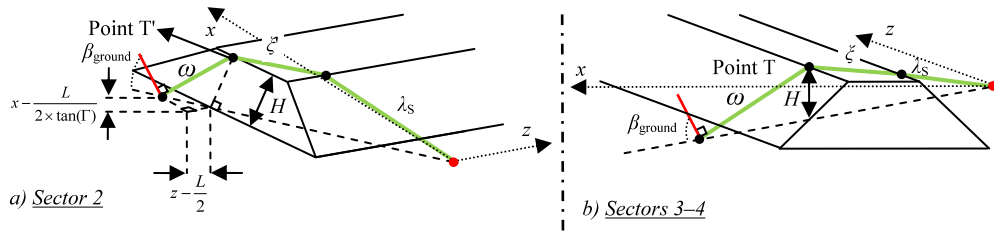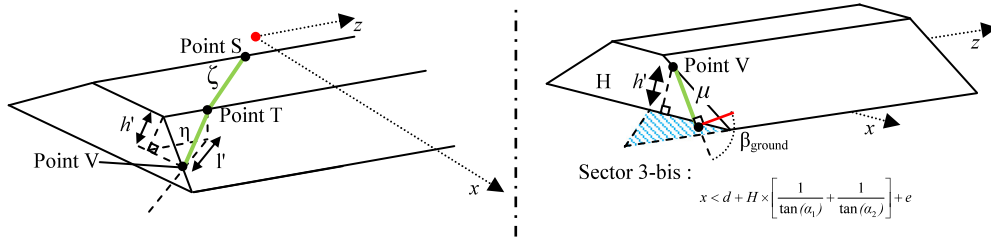**Fig. 12.** Top diffraction and ground reflection.

Fig. 13. Definition of sector 3-bis.

and the kind of reflection requires the knowledge of the straight distance from the source location. Elementary geometric laws are then used. The output diffraction angle, β_s, can then be computed and the diffraction coefficient ($C_{d_{w1}}$) is estimated by our empirical abacus. This approach is followed on each side of the barrier, taking into account previous events to adapt the maximum overpressure. Finally, for any point located at some fractional distance d_w from the source, the direct wave maximum overpressure (ΔP_w^+) is computed as:

$$\Delta P_w^+ = \Delta P_i^+(d_w) \times C_{r_s} \times \prod_k C_{d_{wk}} \times C_{r_{ground}} \tag{14}$$

where C_{r_s} is the reflection coefficient on the front side, $C_{d_{wk}}$ are the generic attenuation coefficients due to diffraction over each crossed edge and $C_{r_{ground}}$ is the final reflection coefficient of the wave on the floor.

One should note that sector 3 may express locally one more diffraction due to the shadowing effect of the lateral back face, see Fig. 13. Sector 3-bis is shown in Fig. 13.

4. Fast-running results

The fast-running model is now applied to the full 3D configuration and compared to the previous experimental and numerical results.

For any ground point of interest, we calculate the distances d_w and d_b from the charge's center for the direct and bypass waves respectively, together with the associated maximum overpressure ΔP_w^+ (14) and ΔP_b^+ (13). The arrival time and the positive phase duration are directly given from formulas (2) and (3), respectively. The temporal pressure signals are then obtained from the Friedlander equation (6) and summed. Doing so, we obtain immediately, i.e. at zero CPU cost, a temporal estimation of the overpressure which can be used for engineering applications. As an example, the profiles at sensors S3 and S6 are plotted in Fig. 14 in comparison with experimental and 3D numerical results. We obtain a fairly good agreement with less than 10% of relative error on the arrival time, but a predicted maximum pressure slightly lower than the CFD calculation. This difference is mainly linked to the second event's arrival time, delayed with our model since waves are assumed unaffected by the preceding events. After the first shock, the sound speed is increased and a modification should be taken into account in a future work. Full results for the others sensors locations are displayed in Table 5. The deviation between the fast-running model and the experiments is 30%, not so far from the CFD results where the overall deviation with the experiments is within 20%. This result could be improved with more evolved fast-running models.

We recall that this fast-running method is intended at specifying zonal effects with regard to the French pyrotechnic regulation, see Table 1. We thus applied it to a 2D spatial grid with a 1-mm uniform stride to create a map of maximum overpressure at the ground level. The code ran about one minute, which should be compared to the equivalent, single CPU, 1800 days for the CFD approach. The final results are shown in Fig. 15. The three most damaging areas, Z1, Z2 and Z3, are in good agreement between both methods. We can note that the 3-bis sector slightly increases the pressure level near the barrier lateral side. At larger distances, the model is known to overestimate the maximum overpressure, which leads to a delayed position of the Z4 to Z5 transition zone. From Eq. (1), one should note that a 30% error on the maximum overpressure leads to nearly the same error on the distance for $\Delta P_i^+ = 0.05$ bar, which is in agreement with the visual results. Nevertheless, this feature is not a limiting point when dealing with the security zone definition.
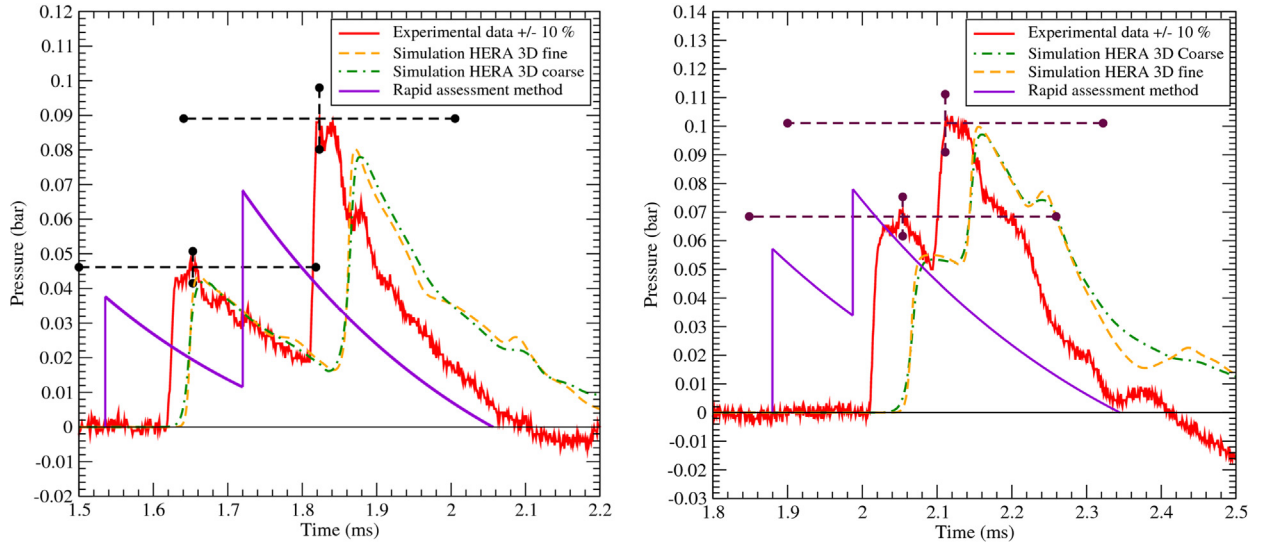
Fig. 14. (Color online.) Temporal evolution of pressure at sensor S3 (left) and S6 (right).

Table 5
Comparison of the maximum overpressure at several locations for the experimental, CFD and fast-running methods.

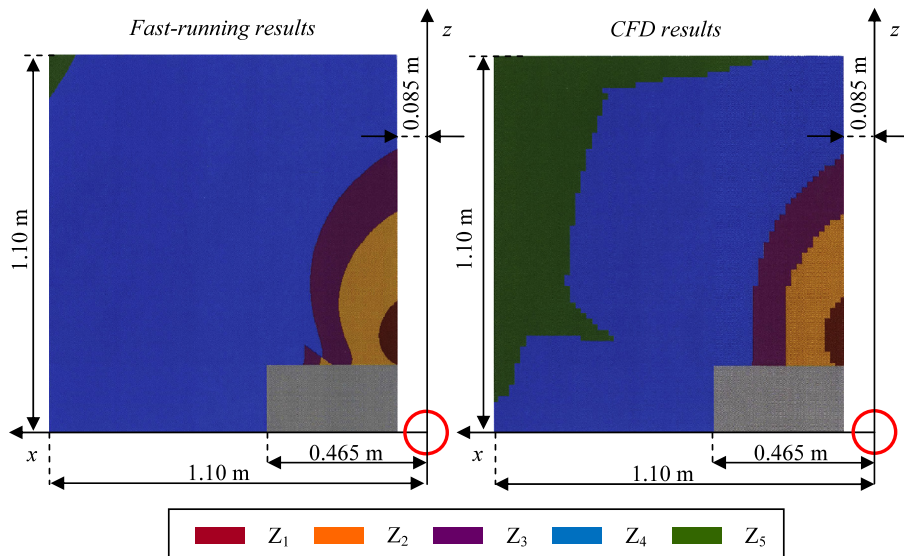| Sensors	Maximum overpressure (bar)			Deviation between		
	Experimental data	CFD 3D fine mesh	Fast-running method	CFD and experimental results	Fast-running and experimental results	Fast-running and CFD
S1	0.124	0.125	0.105	+0.8%	−15.3%	−16.0%
S2	0.087	0.081	0.067	−7.4%	−23.0%	−17.3%
S3	0.089	0.080	0.068	−10.1%	−23.6%	−15.0%
S4	0.107	0.085	0.083	−20.6%	−22.4%	−2.4%
S5	0.091	0.096	0.066	+5.5%	−27.5%	−31.2%
S6	0.101	0.099	0.078	−2.0%	−22.8%	−21.2%

Fig. 15. Top view of the ground effects areas for the fast-running (left) and the CFD (right) methods.

5. Conclusions

The design of a fast-running method, aimed at defining effects areas near protective barriers, has been presented. Small-scale experiments are used first to characterize an explosive gaseous propane–oxygen charge in free field, and then to build a reference 3D, finite-length, protective barrier case. These results helped validating high-resolution Eulerian AMR numerical simulations performed with the HERA code on the TERA-100 supercomputer. From a phenomenological analysis, we suggested a first version of a fast-running method based on geometrical laws combined with reflection and diffraction charts. A simple superposition principle, combined with post-shock pressure decay, was found to be in agreement with the CFD results. In comparison to the experiments, the zero-cost fast-running method introduces an error of -30% at small distance and $+100\%$ at very long ones. The definition of the zonal effect, with regard to the French pyrotechnic regulation, is quite well reproduced for the single studied case. Further work is still needed in order to improve safety engineering practices. In the future, we plan to improve the superposition method by taking into account a variable speed of sound for better second-wave arrival time, and by introducing some new geometrical considerations for wave superposition in order to avoid large-distance overestimations. Finally, other configurations should be tested, particularly for the detonation of chemical explosives such as TNT.

Acknowledgements

References

[1] A. Hadjadj, O. Sadot, Shock and blast waves mitigation, Shock Waves 23 (2013) 1–4.
[2] A.M. Remennikov, A review of methods for predicting bomb blast effects on buildings, J. Battlefield Technol. 6 (3) (2003) 5–10.
[3] GBPP, Guide SFEPA n°9, Guide des bonnes pratiques en pyrotechnie, 2009.
[4] G.F. Kinney, J. Graham Kenneth, Explosive Shocks in the Air, 2nd edition, Springer-Verlag, Berlin, 1985.
[5] Article 11 of the Decree of 20 April 2007 and the circular DPPR/SEI2/IH-07-0111 of the French regulation.
[6] I. Sochet, S. Éveillard, P.-F. Piserchia, J.-Y. Vinçont, Dimensioning physical protection barricades against the propagation of pressure waves following a detonation, in: 13th Interdisciplinary Workshop on Global Security, 22–23rd January 2013, Troyes, France, available online: http://www.agence-nationale-recherche.fr/Colloques/WISG2013/presentations/AAP10_BARPPRO.pdf.
[7] X.Q. Zhou, H. Hao, Prediction of airblast loads on structures behind a protective barrier, Int. J. Impact Eng. 35 (2007) 363–375.
[8] A.M. Remennikov, T.A. Rose, Predicting the effectiveness of blast wall barriers using neural networks, Int. J. Impact Eng. 34 (2007) 1907–1923.
[9] D. Hyde, Microcomputer Programs CONWEP and FUNPRO, Applications of TM 5-855-1, Fundamentals of Protective Design for Conventional Weapons (User's Guide), Final report, 1987.
[10] C.E. Needham, Blast Waves, Springer-Verlag, New York, USA, 2010.
[11] P. Miller, Towards the modeling of blast loads on structures, Thesis for Degree of Master of Applied Science, University of Toronto, Canada, 2004.
[12] S. Trélat, Impact de fortes explosions sur les bâtiments représentatifs d'une installation industrielle, PhD Thesis, University of Orléans, France, 2006.
[13] H. Jourdren, HERA: A hydrodynamic AMR platform for multi-physics simulations, in: Adaptive Mesh Refinement – Theory and Applications, in: Lect. Notes Comput. Sci. Eng., vol. 41, part III, 2005, pp. 283–294.
[14] Tera100, http://www-hpc.cea.fr/fr/complexe/tera.htm.
[15] Ch. Matignon, J.-Y. Vinçont, S. Éveillard, Numerical predictions of blast waves caused by accidental or intentional detonations of gaseous and condensed explosives in 3D complex geometries, in: Proc. 5th Int. Symp. on Tunnel Safety and Security, New York, USA, 2012, pp. 767–768.
[16] N. Desbiens, V. Dubois, C. Matignon, R. Sorin, Improvements of the CARTE thermochemical code dedicated to the computation of properties of explosives, J. Phys. Chem. B 115 (2011) 12868.
[17] G. Ben-Dor, Shock Wave Reflection Phenomena, 2nd edition, Springer, 1991.
[18] U.S. Department of the Army, Structures to Resist the Effects of Accidental Explosions, Army TM 5-1300, Navy NAVFAC P-397, AFR 88-22, Departments of the Army, Navy and Air Force, Washington, D.C., 2008.
[19] Ripley, et al., Small-scale modeling of explosive blasts in urban scenarios, in: 21st Int. Symp. on Ballistics, April 19–23, Adelaide, Australia, 2004, available online: http://hsrlab.gatech.edu/AUTODYN/papers/paper159.pdf.
[20] W. Baker, Explosions in Air, University of Texas Press, Austin, TX, USA, 1973.